IEEE Journal of Microwaves

Received 29 October 2021; revised 14 December 2021, 21 January 2022, 4 February 2022, and 11 February 2022; accepted 14 February 2022. Date of publication 10 March 2022; date of current version 7 April 2022.

Digital Object Identifier 10.1109/JMW.2022.3152208

Sub-6 GHz High FOM Liquid Crystal Phase Shifter for Phased Array Antenna

MOHAMMAD ALI PANAHI, LAP YEUNG (Member, IEEE), MAZIAR HEDAYATI, AND YUANXUN ETHAN WANG (Fellow, IEEE)

(Regular Paper)

University of California Los Angeles, Los Angeles, CA 90095 USA

CORRESPONDING AUTHOR: Mohammad Ali Panahi (e-mail: mpanahi@ucla.edu).

ABSTRACT This paper presents a novel structure based on liquid crystal (LC) technology to achieve a high figure of merit (FOM) phase shifter that works at sub-6 GHz frequencies. The phase-shifting mechanism is enabled through the phase constant variation in the main microstrip line, which is loaded periodically by a variable equivalent capacitance controlled by a bias voltage. Furthermore, a systematic approach based on a transmission line circuit model and the periodic structure theory is developed as a fast method for design optimization by using the ADS and $HFSS$ software. The fabricated phase shifter achieves a maximum insertion loss of 4.35 dB and a maximum phase-shift of 461° at 4 GHz, which indicates an FOM equal to 105.9°/dB. Moreover, the phase shifter return loss is better than –10 dB from 3.7 GHz to 4.2 GHz, covering the sub-6 GHz 5 G band. To validate the performance of the proposed phase shifter, a 1-D electronically steered phased array is designed, fabricated and tested by using a 4 ×4 aperture-coupled patch antenna array, excited by a continuous RF phase-shifting mechanism. The patch antenna array, as a 4-port radiation component, is designed with $HFSS$ full simulation, and achieved a fractional bandwidth of 30% at 4 GHz. The phased array prototype exhibits a continuous beam scanning over the elevation range of 0° to 20°. According to the achieved FOM, and an integrable structure with the printed circuit board (PCB), the proposed low-cost and low power phase shifter is a good candidate for 5G application.

INDEX TERMS Phased array, phase shifter, liquid crystal (LC), patch antenna array, beam steering, beamforming.

I. INTRODUCTION

Fifth-Generation (5G) mobile communication is just around the corner to provide high data-rate and system capacity by using a combination of sub 6-GHz and millimeter-wave frequencies [1]–[2]. To achieve a higher gain and better signal coverage in 5 G mobile communication, advanced phased array or multi-beam antenna systems have been developed [3]–[4]. Phased arrays have been traditionally used in military applications for several decades. However, there are still major constraints against using them in commercial applications, and these include their high cost, power consumption, and high hardware complexity. To use the phased array in commercial applications, there is a need for low-cost, low power, and low-weight tunable phase-shifters as a key component. The performance of different phase shifters is summarized further in Table 3. To compare their electrical performance, the classical figure of merit (FOM) [5] is used as the ratio of the maximum differential phase shift and the maximum insertion loss, as given in (1).

$$FOM = \frac{\triangle\phi_{max}}{IL_{max}} \tag{1}$$

Phase shifters can be classified into two categories: active and passive [6]–[7]. Active phase shifters provide gain, while having more power consumption and introducing more non-linearity to the system. Vector modulators (VMs) are one of the most common active phase shifters, used in applications which do not require high resolution and high

TABLE 1. The Primary Specified Parameter to Design MLCPS

f_0	4 GHz	h_G	700 μm
f_B	27 GHz	h_{LC}	4 μm
Z_0	28 Ω	$\varepsilon_{r,\parallel}$	3.77
Z_{BU}	16 Ω	$\varepsilon_{r,\perp}$	2.7
$tan\ \delta_{\parallel}$	0.005	$tan\ \delta_{\perp}$	0.012
t	1.3 μm	ε_{reff}	1

TABLE 2. Final Optimized Dimensions of the Proposed MLCPS

W_m	2.5 mm	W_S	1.2 mm
P	0.95 mm	l_S	500 μm
l_{GS}	620 μm	L_{tr}	12.2 mm
a	245 μm	b	310 μm
W_{GS}	1.9 mm	W_{tr}	5.55 mm
W_{in}	1.1 mm	L_{in}	5 mm

dynamic range. In the vector modulator structure, the input signal is divided by two signals with quadrature phase in a quadrature generator (QG). Then, the amplitude of each signal is scaled with variable gain amplifier (VGA), and finally a combiner adds two signals to achieve the desired phase shift [8]. Passive phase shifters can achieve more power handling for large input signal with lower power consumption but exhibit higher insertion loss. To achieve a low insertion loss, an optimized phase shifter topology can be implemented by different technologies of CMOS, BiCMOS, Barium Strontium Titanate (BST), Liquid Crystal and micro-electromechanical system (MEMS). Three conventional topologies are considered to design passive phase shifters, which are reflection-type phase shifter ($RTPS$), loaded transmission line phase shifter ($LTPS$), and switched transmission line phase shifter ($STPS$) [6]–[7]. The RTPS is based on a 90° hybrid coupler connected to a load, like a varactor diode, which is varying continuously to create the phase shift. In [9], a new switched inductor load structure is proposed to have a simple and low power control voltage block in the RTPS with an average insertion loss of 9.5 dB at 29 GHz. RTPS can achieve high resolution; however, varactor quality factor, Q, and loss vary across capacitance settings, leading to insertion loss variation with the phase shift. This loss variation results in a nonuniform amplitude distribution in phased array antennas and increases the side lobe-level. The LTPS topology is based on a transmission line loaded periodically with shunt or series loads, which are tuned to obtain a phase shift. A transmission line loaded periodically with MEMS bridge is proposed in [10], and a FOM of $150^\circ/dB$ was achieved. MEMS may need expensive packaging to protect the movable MEMS bridges against the environment. In the STPS, the RF signal propagation length is switched between delay lines of different physical length, which is implemented with p-i-n diode, MOS-FET or MEMS switches. By using an improved switching time CMOS transistor, a low loss STPS was achieved in [11]. A drawback of the STPS is phase resolution limitation, generated by the number of the transmission lines and switches, which is in trade-off with the insertion loss. Another way to make phase shifters based on transmission lines is to use materials with controllable permittivity and permeability, like ferroelectric or ferrite, as a substrate. A phase shifter implemented with GCPW line under barium strontium titanate (BLT) accomplished a high FOM of $221.4^\circ/dB$ [12]. Even though these materials lead to high FOM phase shifters, they need a high driving voltage or power and high fabrication costs.

Liquid crystals (LCs) are controllable dielectrics which demonstrate large electrically controlled birefringence in the microwave frequency domains. They are planar in shape, low power, low loss and especially low cost because they are fabricated using the conventional Liquid Crystal Display (LCD) manufacturing technology. Nematic LCs [13] are a type of tunable anisotropic dielectric whose properties could be controlled by using surface anchoring, or an external electric or magnetic fields. Nematic LCs possess relatively low dielectric loss in the microwave frequency range, require low operation voltage, and have continuous tuning ability. They have become more and more widely used in various microwave applications, such as phase shifters [14]–[18]. There are various designs for LC-based phase shifters, mostly in millimeter-wave frequencies. A 2-D phased-array antenna with LC-based variable delay lines is presented in [19], and the FOM achieved was $62.5^\circ/dB$ at 17.5 GHz. A tunable liquid crystal phase shifter based on periodically loaded CPW transmission line is proposed in [20], and the FOM achieved was $60^\circ/dB$ at 20 GHz. The dielectric loss tangent of LC material decreases with an increasing frequency, and LC's generally exhibit their highest performance at frequencies above 10 GHz [21]. This is the reason that most LC-based phased shifters have been proposed in the millimeter-wave frequencies; that way, they achieve higher FOM. Even though many topologies have been well developed at millimeter-wave frequencies, they suffer from RF loss in the frequencies lower than 10 GHz. Thus, to design a LC-based phase shifter at low frequencies, a new topology is still necessary to reach a high FOM in sub-6 GHz applications. In this paper, a novel structure for LC-based phase shifter ($LCPS$) is proposed, which achieves an FOM of $105.9^\circ/dB$ at 4 GHz while the insertion loss is roughly constant over the operational bandwidth. In the previous LTPS [20], the main transmission line, with a characteristic impedance higher than 50 Ω, is loaded directly with a shunt capacitance by using one tuning stub. In the proposed novel structure for LCPS, the lower than 50 Ω microstrip line is used to have a bigger line width and lower ohmic loss, while the 50 input matching is implemented with a tapered transmission line. To increase the phase shift in the proposed LCPS, the main low impedance transmission line is periodically loaded with an equivalent capacitance created with two series tuning stubs. These two stubs allow us to achieve a higher loaded capacitance compared with the directly loading shunt capacitance with one tuning stub [20], resulting a higher FOM.

This paper is organized as follows. In Section II, part A, the phase shifter structure is described in detail with dimensions and unknown variables. In Section II, part B, a circuit model is presented, and a theory is developed to derive the equations

TABLE 3. Phase Shifter State-of-the-Art

Technology	Topology	Freq. (GHz)	Delta	Gain	FOM	Power Handling (dBm)	Drive Voltage, Power	Area (mm2)	Ref.
CMOS 65nm	Active, VMPS [1] with Gain Amplifier	25	360	+12.2	\	$\leq$ 10 dBm	12mW	0.052	[8]
CMOS 65nm	Passive, RTPS [2]	29	360	-9.5	37.9	$\leq$ 30 dBm	0 DC power	0.23	[9]
PCB	Passive, RTPS	2	407	-4.4	88	$\geq$ 30 dBm	5 V	4000	[28]
MEMS on PCB	Passive, STPS [3]	2.7	75	-89	84	$\geq$ 30 dBm	N.A	400	[29]
MEMS	Passive, LTPS [4]	30	270	-1.8	150	$\geq$ 30 dBm	16 V	30	[10]
CMOS 65 nm	Passive, STPS	28	360	-6.36	56.6	$\leq$ 10 dBm	1 V	0.23	[11]
Ferroelectric (BLT [5])	Passive, GCPW line under BLT slab	20	210	-1.4	221.4	$\gg$ 30 dBm	22mW	60	[12]
Ferrite on PCB	Passive, Microstrip line under Ferrite	3.3	679.9	-30	22.6	$\gg$ 30dBm	100 KA/m	3551	[30]
Liquid Crystal	Passive, Microstrip delay line	17.5	N.A	-4	62.5	$\geq$ 30 dBm	25 V	350	[19]
Liquid Crystal	Passive, CPW LTPS	20	90	-1.5	60	$\geq$ 30 dBm	40 V	NA	[20]
Liquid Crystal	Passive, Microstrip LTPS	17	30	-1	30	$\geq$ 30 dBm	20 V	NA	[31]
Liquid Crystal	Passive, Loaded Dielectric Waveguide	75	360	-3.6	100	$\geq$ 30 dBm	250 V	112.5	[32]
Liquid Crystal	Passive, Microstrip RTPS	35	270	-7	38.5	$\geq$ 30 dBm	25 V	NA	[33]
Liquid Crystal	Passive, Microstrip LTPS	28.4	400	-7.4	54	$\geq$ 30 dBm	5 V	NA	[34]
Liquid Crystal	Passive, A novel LTPS architecture	4	461	-4.31	105.9	$\geq$ 30 dBm	0 DC power, 20 Vp-p	616	This Work

[1] Vector Modulator Phase Shifter, [2] Reflection-Type Phase Shifter,
[3] Switched Transmission Line Phase Shifter, [4] Loaded Transmission Line Phase Shifter,
[5] Barium Strontium Titanate

needed for designing the microstrip line LCPS. In Section II, part C, the LCPS design algorithm is described step-by-step by using the equations derived in part C. In Section II, part D, the LCPS measurement results are shown, which shows a good FOM of $105.9^\circ/dB$ at 4 GHz. To study the performance of the proposed phase shifter, a phased array is designed and implemented by using a 4×4 aperture-coupled patch antenna arrays in Section III. In addition, the phased array calibration is explained, and measurement results are presented, confirming the performance of proposed phase shifter. Finally, a conclusion is given in Section IV.

II. LC PHASE SHIFTER THEORY, DEIGN, AND MEASUREMENT

A. MICROSTRIP LINE LCPS STRUCTURE

The proposed Microstrip line LC-based phase shifter (*MLCPS*) is shown in Fig. 1. The phase shifter structure is implemented by two glass layers as a substrate with thickness of h_G, and a Nematic liquid crystal as a tunable dielectric is contained between them with a fixed thickness of h_{LC}. As shown in Fig. 1(a), the MLCPS is a two-port component, which consists of a main microstrip transmission line loaded with a shunt stub, creating a periodic structure with 80 unit-cells to reach 360° phase-shift. To match the input impedance of the periodic structure to 50 Ω, a microstrip line transition is used at the MLCPS input and output. The MLCPS unit-cell with specified dimensions is shown from top view in Fig. 1 b, and from the cross section in Fig. 1 c. Each unit-cell consists of a copper-based main microstrip line deposited on the top-surface of glass$_1$, and a copper-based microstrip ground implemented on bottom-surface of glass$_1$. The microstrip line width and thickness is defined with W_m and t respectively. In each unit-cell, the main microstrip line is connected to the red-colored microstrip line stub, which is specified with the dimension of (t, W_s, l_s) in the direction of X, Y, and Z respectively. A green pad shown in Fig. 1 b with the dimension of $a * b$, is connected to the red-colored

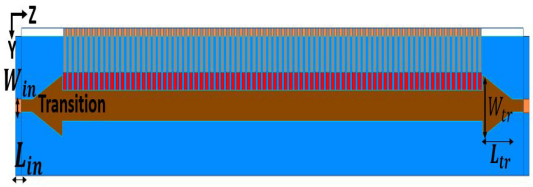

(a) 80 unit-cells with impedance matching transition top-side view

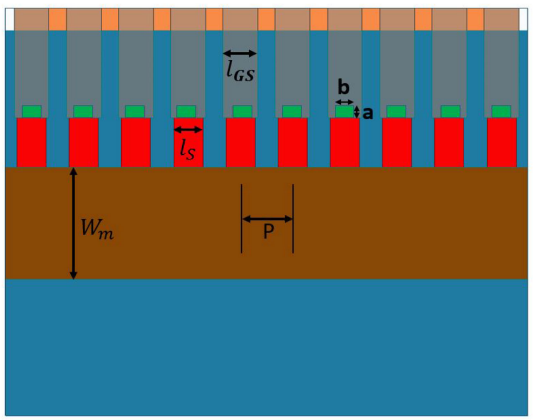

(b) 10 unit-cells top-side view

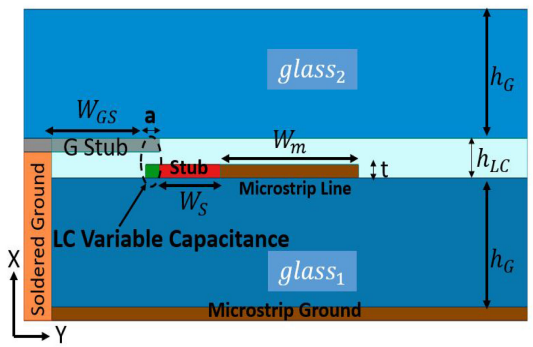

(c) Cross-side view

FIGURE 1. Proposed Microstrip line LCPS structure constructed by a microstrip line periodically loaded by a variable equivalence capacitance.

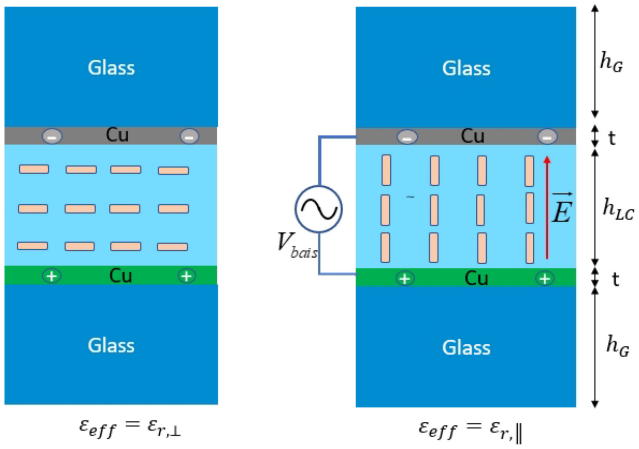

FIGURE 2. Variable capacitance shown in Fig. 1c, is created by a sandwiched LC material between two electrodes for applying electric field. The effective permittivity of the LC material is changed from (a) when there is no external bias voltage, to (b) when saturated bias voltage is applied.

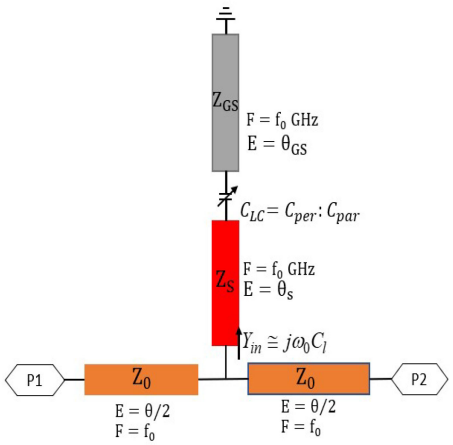

FIGURE 3. Distributed transmission line model of the MLCPS unit-cell, assuming the variable LC capacitance shown in Fig. 1 and 2 can be representative by C_{LC}.

stub on the top-surface of glass$_1$. This green pad has an intersection with the microstrip line G-stub deposited on the bottom-surface of glass$_2$, making an LC-based parallel-plate capacitance like a bridge, as shown in Fig. 1 c with a dash line. The G-stub is used to connect the LC parallel-plate capacitance to the main microstrip ground by using a soldered ground connection implemented on the edge of glass$_1$. The G-stub has a width W_{GS}, a length l_{GS} and a thickness t. The length of each unit-cell P is a periodic spacing in MLCPS structure.

Fig. 2 describes the usage of LC parallel-plate capacitance, shown with the dash-line in Fig. 1 c, and how to make a variable LC capacitance for phase-shifting mechanism. The LC material sandwiched between two copper plates as an electrode, consists of uniaxial anisotropic molecules [22]. When the external bias voltage between the copper electrodes is zero, the LC molecules are aligned perpendicularly to the RF field, as shown in Fig. 2 a. In this perpendicular case, the effective permittivity ε_{eff} and loss tangent $\tan\delta$ seen by the RF field are equal to $\varepsilon_{r,\perp}$ and $\tan\delta_{\perp}$, respectively. The LC molecules are aligned parallel to the RF field when an external bias voltage that is larger than the saturated voltage V_{sat} is applied between the copper electrodes, as shown in Fig. 2 b. In this parallel case, the effective permittivity ε_{eff} and loss tangent $\tan\delta$ experienced by the RF field are equal to $\varepsilon_{r,\parallel}$ and $\tan\delta_{\parallel}$, respectively. By controlling the external bias voltage applied to the electrodes from 0 to V_{sat}, the effective permittivity of the parallel-plate capacitance is changed from $\varepsilon_{r,\perp}$ to $\varepsilon_{r,\parallel}$ as a function of LC molecules orientation. This mechanism results in a variable capacitance controlled by the external bias voltage. The upper LC capacitance electrode is connected to the main microstrip ground, which is used as the bias voltage ground too. The lower LC capacitance electrode is connected to the main microstrip line. Therefore, to excite the phase shifter with the bias voltage and the RF signal simultaneously, a Bias-Tee microwave component is used to add the external bias voltage to the RF-INPUT. Thus, the variable capacitance controlled by the bias voltage is loaded to the main transmission line and will cause a phase shift in the phase shifter by changing the phase constant.

B. MICROSTRIP LINE LCPS THEORY

To analyze and design the proposed MLCPS, the distributed circuit model is very useful. Each of the MLCPS unit-cell is modeled with transmission lines and is shown in Fig. 3. The main microstrip transmission line shown with width W_m and length P, in Fig. 1 b, is modeled as a transmission line with a characteristic impedance of Z_0 and an electrical length of θ° at the center frequency of f_0. The red-colored stub and G-stub are modeled as transmission lines with characteristic impedance and electrical lengths of Z_s, $\theta_s{}^{\circ}$, Z_{GS} and $\theta_{GS}{}^{\circ}$. The LC variable capacitance is modeled with C_{LC}, which varies from C_{per} to C_{par} when LC molecules rotate from perpendicular case to parallel case. The LC variable capacitance can be loaded directly with one stub to the main transmission line [20]; however, it is loaded indirectly between two stubs like a bridge in each MLCPS unit-cell, as shown in Fig. 1–3. The stubs$'$ electrical length $\theta_S{}^{\circ}$, and $\theta_{GS}{}^{\circ}$, are finally tuned in a way to see roughly capacitive admittance $j\omega_0 C_l$ from the input of loaded stubs. These two stubs allow us to have more flexibility in design, and to reach a bigger equivalent loaded capacitance C_l from LC variable capacitance C_{LC}, resulting in a higher FOM. The unit-cell transmission line model, shown in Fig. 3, is simplified and modeled with lump-elements in Fig. 4. The loaded shunt capacitance C_l varies from C_{lu} to C_{lb}, when the bias voltage increased from the minimum to the saturation voltage V_{sat}. The ratio of maximum loaded capacitance to the minimum loaded capacitance C_r is given in (2). This ratio is a function of parallel to perpendicular case relative permittivity, since the other parameters in the loaded

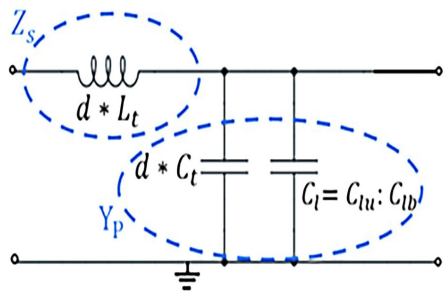

FIGURE 4. Lumped-element transmission line model of the MLCPS unit-cell shown in Fig. 3, assuming the input admittance shown in Fig. 3 can be representative by a shunt capacitance C_l.

capacitance are constant.

$$C_r = C_{lb}/C_{lu} \cong \varepsilon_{r,\parallel}/\varepsilon_{r,\perp} \tag{2}$$

The main microstrip transmission line, defined with Z_0 and θ° in Fig. 3, is modeled with per unit length inductance L_t and capacitance C_t. The value of L_t and C_t are driven based on the value of Z_0, given by [23]

$$C_t = \frac{\sqrt{\varepsilon_{reff}}}{v_c Z_0} \; and \; L_t = C_t Z_0^2 \tag{3}$$

in which ε_{reff} is the effective dielectric constant of the transmission line with the characteristic impedance Z_0, shown in Fig. 3, and v_c is the free space velocity. The proposed *MLCPS* is modeled with distributed lump-elements by cascading the unit-cell model represented in Fig. 4. The input Bloch impedance of this periodically loaded line for the un-biased case is given by [24]–[25].

$$Z_{BU} = \sqrt{\frac{Z_s}{Y_p}}\sqrt{1-\left(\frac{\omega}{\omega_B}\right)^2} = \sqrt{\frac{d^*L_t}{d*C_t + C_{lu}}}\sqrt{1-\left(\frac{\omega}{\omega_B}\right)^2} \tag{4}$$

where ω_B is the Bragg frequency and given by [24]–[25]:

$$\omega_B = 2/\sqrt{d*L_t(d*C_t + C_{lb})} \tag{5}$$

By using the equations (2), (4) and (5), the periodic length of each unit-cell d, and the un-biased loaded capacitance C_{lu}, is determined and represented by equation (6) and (7).

$$d = \frac{Z_{BU}}{\pi f_B \sqrt{L_t(C_r L_t - (C_r - 1)C_t {Z_{BU}}^2)}} \tag{6}$$

$$C_{lu} = d\left(\frac{L_t}{{Z_{BU}}^2} - C_t\right) \tag{7}$$

The phase shift per unit length is calculated from the change of phase constant experienced by the external bias voltage [25]:

$$\Delta\phi = \omega\sqrt{L_t C_t}\left(\sqrt{1+\frac{C_{lb}}{d*C_t}} - \sqrt{1+\frac{C_{lu}}{d*C_t}}\right) \tag{8}$$

C. MICROSTRIP LINE LCPS DESIGN

To design the phase shifter proposed in Fig. 1, the primary parameters are defined and shown in Table 1. The center frequency of 4 GHz and 50 Ω input-matching with bandwidth of 500 MHz, are aimed to support the 5G applications in Sub-6 GHz channel. A glass material with relative permittivity of 4.8 and loss tangent of 0.007 is used for MLCPS substrate. The external bias is a function of LC material type. The relative permittivity of the used LC material is changed from the perpendicular case ($\varepsilon_{r,\perp}$ =2.7) to the parallel case ($\varepsilon_{r,\parallel}$ =3.77), when the peak-to-peak bias voltage amplitude varies from 2 to 20 V_{p-p}. There is no phase shift response between 0 V and 2 V, so the measurement is reported from 2 to 20 V_{p-p}. The maximum phase shift is accomplished in MLCPS, when a rectangular pulse with a frequency of 277 Hz is applied as an external bias. The LC material permittivity response depends on the external bias voltage and frequency. For the LC material used in the proposed LCPS, the biggest phase shift response is achieved in the measurement with the drive frequency of 277 Hz. In the proposed novel structure for LCPS, the main microstrip line, with a characteristic impedance Z_0 lower than 50 Ω, is used to have a bigger line width and lower ohmic loss, improving the FOM.

The first step is to calculate the main microstrip line parameters and loaded capacitance values, shown in Fig. 4. By using the primary parameters given in Table 1 and the (3), the per unit length inductance L_t and capacitance C_t are calculated. By using these calculated values and the primary parameters given in Table 1, the periodic unit-cell length d, is defined by the equations of 2 and 6. By using the calculated values of C_r, L_t, C_t, d, and the input Bloch impedance given in Table 1, the minimum loaded capacitance and the maximum loaded capacitance will be calculated.

The second step, in designing the MLCPS, is finding the value of the stubs and the LC variable capacitance C_{LC} between them, as shown in Fig. 3. To make our design more convenient with faster optimization in ADS software, an ideal transmission line with $\varepsilon_{eff} = 1$ is assumed in the beginning for all the transmission lines. A 10 unit-cell network, which is created by cascading the two-port circuit model shown in Fig. 3, is used in ADS optimization. The stubs' values including Z_s, $\theta_S{}^\circ$, Z_{GS}, $\theta_{GS}{}^\circ$, and the LC variable capacitance C_{LC}, are calculated by doing the optimization in ADS. The ADS optimization goal is to make the minimum and the maximum input admittance Y_{in} equal to $j\omega_0 C_{lu}$ and $j\omega_0 C_{lb}$, which have been calculated in the second step. The main microstrip line characteristic impedance Z_0 is given in Table 1, and its electrical length θ will be calculated by $\theta = (\frac{2\pi}{\lambda_0}) * d$, where d is the unit-cell length, derived in the first step. All the parameters in the 10 unit-cell networks, created by cascading the two-port circuit model, are now defined. These known variables are tuned in ADS to achieve the best FOM while the input impedance is matched to Z_{BU}.

In the third step or final step, the ADS optimized values achieved in the second step are converted in HFSS software to find the variables in Fig. 1. By having the lines' characteristic

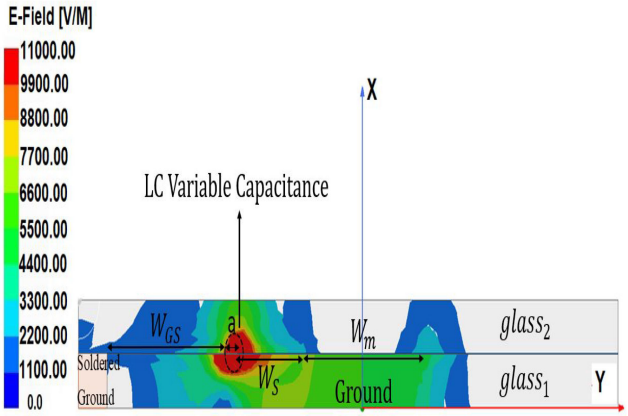

FIGURE 5. HFSS simulated magnitude of E-field on the cross-side view shown in Fig. 1c.

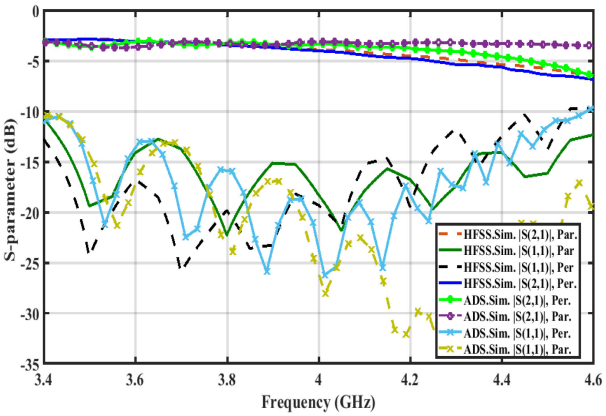

FIGURE 6. S-parameter of the proposed MLCPS versus frequency, calculated with the HFSS full-wave simulation and ADS circuit model simulation, for the perpendicular and parallel case.

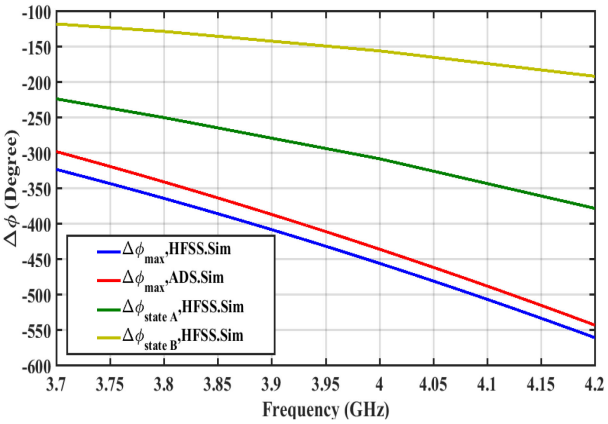

FIGURE 7. The maximum state ($\varepsilon_r = 3.77$), state A ($\varepsilon_r = 3.3$) and state B ($\varepsilon_r = 2.9$) phase-shift relative to the minimum state ($\varepsilon_r = 2.7$), calculated with the HFSS full-wave simulation and ADS circuit model simulation.

impedance of Z_0, Z_s, and Z_{GS}, the lines' width and their propagation constant β are defined in the HFSS model. Next, the optimized electrical lengths from the second step including θ°, $\theta_S{}^\circ$, and $\theta_{GS}{}^\circ$, are converted to the lines' dimensions P, W_S, and W_{GS} respectively, based on their related propagation constant. The LC variable capacitance dimensions a, and b, are defined based on the optimized C_{LC} calculated in the second step.

The two-port network of 10 cascaded unit-cells, shown in Fig. 1(b), are optimized in HFSS to have the highest FOM and input matching to Z_{BU} concurrently. To reach a full cycle of phase shift, 360°, 80 unit-cells are implemented in the final MLCPS prototype. A microstrip line transition with dimensions of W_{tr} and L_{tr} is used to match the input impedance of Z_{BU} to 50 Ω. The input impedance of the loaded transmission line without the matching section (Z_{BU}) varies from 16 Ω to 11.7 Ω, while the bias voltage changes from the minimum (2 V_{P-P}) to the maximum value (20 V_{P-P}). The final optimized dimensions of the proposed MLCPS are given in Table 2. The HFSS simulated magnitude of E-Field on the cross-side view of MLCPS is shown in Fig. 5. The S-parameter of the proposed MLCPS versus frequency, calculated with the HFSS full-wave simulation and ADS circuit model simulation, is shown in Fig. 6. The maximum phase shift of the proposed MLCPS versus frequency, calculated with the HFSS full-wave simulation and ADS circuit model simulation, is shown in Fig. 7. The insertion loss lower than 3.95 dB and maximum phase shift of 456.2° are achieved at 4 GHz in the HFSS simulation. The insertion loss lower than 3.35 dB and maximum phase shift of 435° are achieved at 4 GHz in the ADS simulation.

D. MICROSTRIP LINE LCPS MEASUREMENT

The prototype of the proposed MLCPS is shown in Fig. 8. The structures dimensions and specifications are given in Table 1 and 2. As illustrated in Fig. 8, the MLCPS is constructed with two layers of glass as a substrate which are attached together in a way that hold the LC material between them. The main microstrip line, loaded periodically with the stubs, is connected to the 50 Ω SMA connector after the microstrip line impedance matching transition. A copper tape, attached to the bottom of glass1 as a main ground, is soldered from the edge (Fig. 8(b)) to the $glass_2$, including the periodic metal G-stubs.

The measured S-parameter of the manufactured phase shifter is shown in Fig. 9. The LC loss varies somewhat linearly from the minimum bias to the maximum bias. The two-port device shows a minimum insertion loss of 3.82 dB and a maximum insertion loss of 4.35 dB for different bias states at center frequency of 4 GHz. The insertion loss at different states are between these two values. In addition, the phase shifter prototype is well matched to 50 Ω from 3.1 GHz to 4.9 GHz, covering the 5G sub-6 band. To measure the phase-shift through the MLCPS, we have used an RF Bias Tee component in series with the phase shifter input to simultaneously apply the RF input and the external bias voltage. A rectangular-shaped pulse with a frequency of 277 Hz is used as an external bias voltage. The measured phase-shift in degrees at 4 GHz versus the applied bias voltage is shown

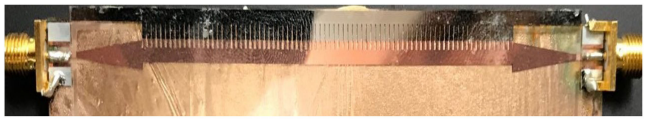

(a) Top-side view

(b) Bottom-side view

FIGURE 8. Manufactured prototype of the proposed MLCPS. (a) Top-side view including a main microstrip transmission line loaded with a variable equivalence capacitance. (b) Bottom-side view including a copper-tape as a main ground, which is soldered from the edge to make a connection with the loaded periodic stubs.

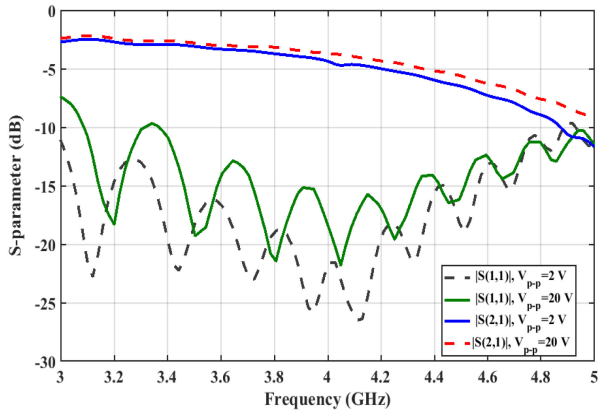

FIGURE 9. Measured S-parameters of the proposed MLCPS.

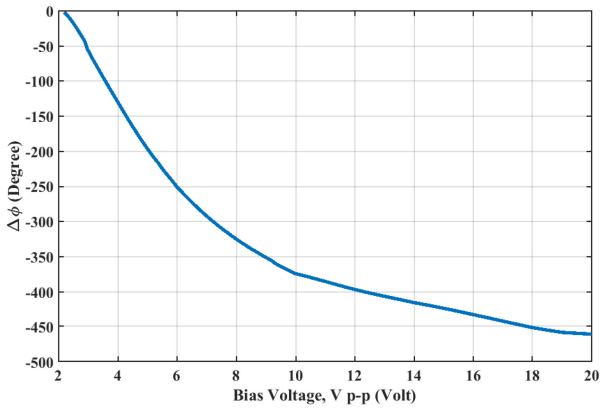

FIGURE 10. Measured phase-shift of the proposed MLCPS versus the peak-to-peak bias voltage at 4 *GHz*, which is a rectangular-shape pulse with the frequency of 277 *Hz*.

in Fig. 10. By increasing the peak-to-peak bias voltage from 2 to 20 Volts, the amount of phase-shift is increased, and finally a 461° phase-shift is achieved at 20 $Vp-p$. Based on the phase shifter FOM definition given in (1), the proposed MLCPS achieved $105.9°/dB$ at 4 GHz. This MLCPS has $5.76°/mm$ with the tuning speed of 2 msec. To evaluate the linearity, the two-tone test output power spectrum is measured

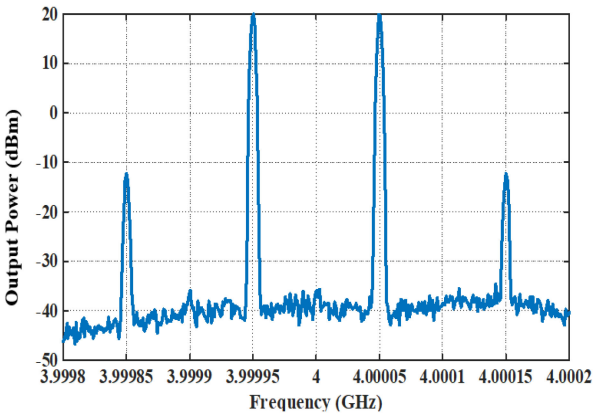

FIGURE 11. Measured two-tone test power spectrum for MLCPS.

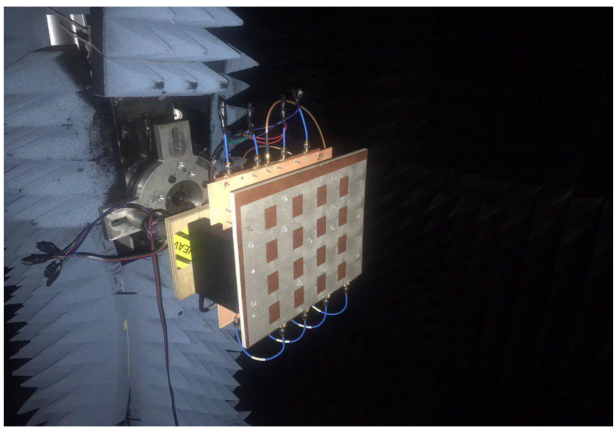

FIGURE 12. RF phase-shifting phased array pattern measurement set-up, by using a 4×4 aperture coupled patch antenna array and a 1×4 proposed phase shifter.

and shown in Fig. 11, resulting the OIP3 of 36.1 dBm. There is not any LC-based phase shifter at such a low frequency in the literature which to compare our design, but this result compares with phase shifters designed in the millimeter-wave frequencies, reported in [19]–[20].

III. LC-BASED PHASED ARRAY DESIGN AND MEASUREMENT

In this section, a RF phase-shifting phased array system is designed and implemented, as shown in Fig. 12, to verify the performance of the proposed MLCPS. The phased array system includes an antenna array panel and four-phase-shifter panel, assembled behind the antenna array to make a relative phase-shift in each RF path. The antenna array is constructed with 4×4 aperture-coupled patch antenna elements. By using the equations in [26], the antenna array is designed and optimized in HFSS to cover the sub-6 GHz band, 3.7GHz to 4.2 GHz. The aperture-coupled patch antenna with optimized dimensions is shown in Fig. 13 a and b. The radiating patch element is etched on the top of the antenna substrate (AD250c), and the microstrip 50 Ω transmission line is etched on the bottom of the feed substrate (RO4003c). The AD250c has a

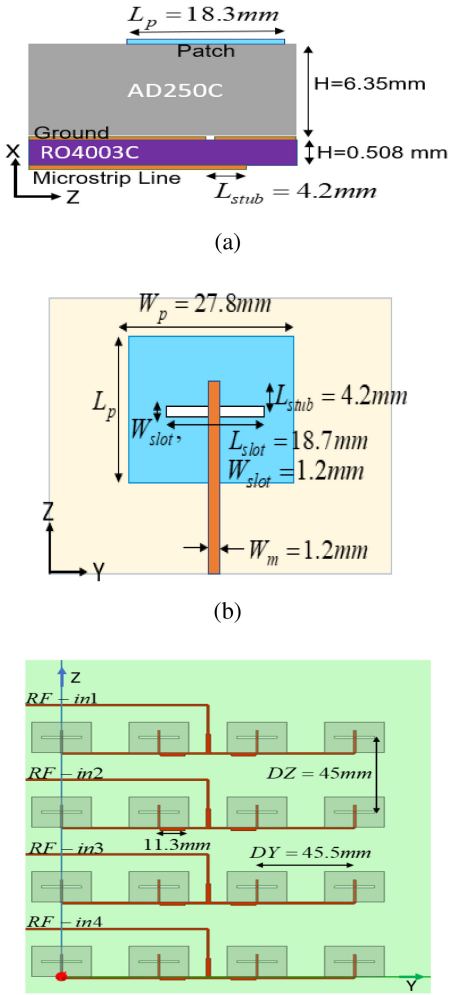

FIGURE 13. A 4×4 aperture coupled patch antenna array. The patch antenna element designed at 4 *GHz*, is shown from (a) Side view, and (b) Top view with related dimensions. (c) 4 sub-arrays placed in *Z* direction, is created by exciting 4 patch antenna elements placed in *Y* direction.

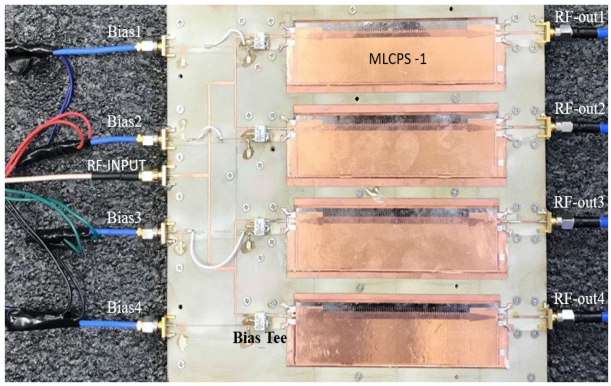

FIGURE 14. 1×4 array of the proposed MLCPS assembled on the Rogers board with a Bias Tee chip to apply the bias voltage with RF field.

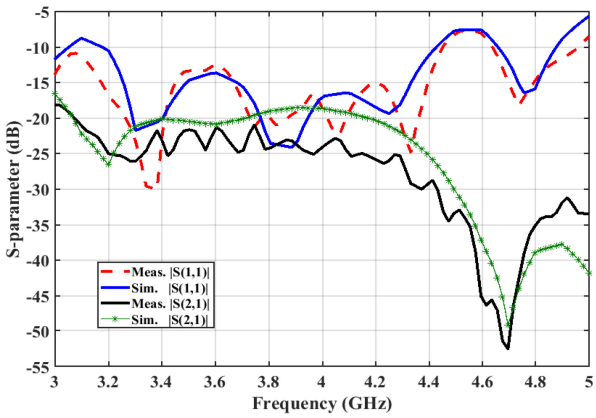

FIGURE 15. Input matching and mutual coupling of the 4-port aperture-coupled patch antenna array, as shown in Figs. 8 and 9.

dielectric constant of 2.52 and loss tangent of 0.0015. The patch length (L_p) and width (W_p) is determined to resonate at the operational center frequency. The coupling level is primarily determined by the length of the coupling slot (L_{slot}), and the tuning stub (L_{stub})is used to tune the excess reactance of the slot coupled antenna, achieving the 50 Ω input matching. As shown in Fig. 13 c, each 4 patch antennas are placed in Y direction with interelement spacing $DY = 45.5\,mm$, and are uniformly excited with the microstrip line, which make four antenna sub-arrays. The antenna sub-arrays are placed in Z direction with spacing $DZ = 45\,mm$, creating a 4-port radiation component. The input matching and the radiation coupling of the 4-port antenna array are shown in Fig. 15, resulting in 50 Ω matched ports from 3.2 GHz to 4.4 GHz.

The phase shifter panel shown in Fig. 14, includes 1-to-4 microstrip line power divider to feed the *RF* field of each phase shifter, mounted on the *RO*4003 board. This board has a thickness equal to the phase shifter's glass, and is cut inside to hold the phase shifter. The ground of the phase shifter is connected to the Rogers board ground layer with copper tape to have a shared ground. The microstrip line on the Rogers board is connected to the phase shifter line by soldering. To combine the RF field and bias voltage, and to control the amount of phase-shift in each phase shifter, four Mini-Circuits model RCBT-63+ bias tees are integrated at each RF path. The external bias voltages are applied to each Bias Tee from four separate ports, as labeled in Fig. 14 from Bias1 to Bias4. The RF-INPUT signal is divided into 4 RF-path signals and is added with the bias voltage in the bias tee chips, to excite the phase shifter in each RF path. After being phased shifted in each MLCPS, the four phase-shifted RF signals, Fig. 14, are connected to the antenna array four input ports with the coaxial cable, Fig. 13 c and Fig. 12.

The amount of phase-shift needed to have a steered pattern to θ, is given in [27]. To find the bias voltage for each RF pass, the phased array is calibrated by Agilent Network Analyzer (VNA). By applying the external bias voltages in the set-up shown in Fig. 12, the simulated and the measured normalized radiation patterns are defined and shown in Fig. 16, and 17.

The measured radiation patterns are matched with the simulated patterns in all cases with some discrepancies especially

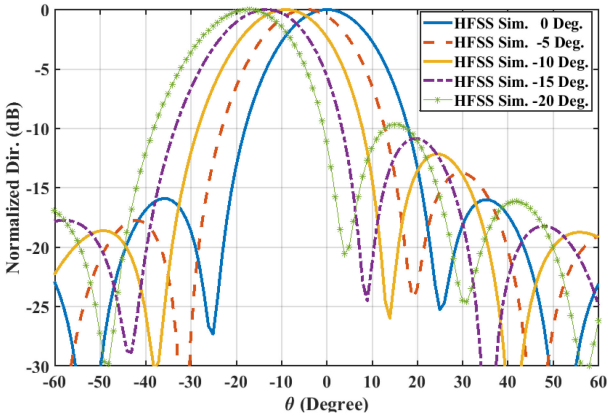

FIGURE 16. Simulated normalized radiation pattern of the phased array at 4 *GHz* for various beam steering.

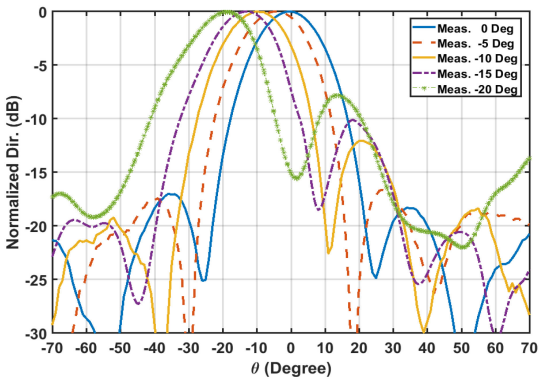

FIGURE 17. Measured normalized radiation pattern of the phased array at 4 *GHz*.

in sidelobes. This is because of the dissimilarities between the phase shifters' performance created due to the fabrication inaccuracies, which results a non-uniform feeding network in the antenna array. The antenna array peak gain shows 18.1 dBi at the boresight for the HFSS simulation and 17.3 dBi for the measurement. Nonetheless, the measured result proves the performance of the proposed LC-based phase shifter.

The MLCPS experimental results are compared with the recent phase shifter state-of-art in Table 3. As shown in Table 3, the proposed phase shifter achieves a high FOM of $105.9°/dB$ with a full cycle of phase shift. Besides that, the proposed architecture could be integrated on the PCB board which enables it to be assembled with the antenna platform. In addition, the insertion loss variation with the phase shift is much smaller than the RTPS [9], and the accessible phase resolution is much higher than the STPS [11]. The other parameters of the phase shifter reported in Table 3 are either better than or on par with that of previously reported works.

IV. CONCLUSION

In this paper, a new structure is proposed for the LC-based phase shifter to achieve a higher FOM at sub-6 GHz frequencies, which are necessary for 5G applications. The proposed structure is based on the microstrip transmission line loaded periodically with the equivalent capacitance seen from the shunt stubs. A theory is developed to design and optimize the proposed phase shifter. By using the derived equations in the theory section, along with ADS and HFSS simulation, the phase shifter is designed at 4 GHz, and it achieves the FOM of $105.9°/dB$ and input matching from 3.7 GHz to 4.2 GHz. To verify the performance of the proposed phase shifter, a phased array system has been implemented by using the aperture-coupled patch antenna array. The measured radiation pattern of the phased array prototype validates the performance of the proposed phase shifter. Due to the planar shape and low-cost fabrication process available in LCD technology, the proposed phase shifter with its good FOM will be a potential candidate for 5G applications.

REFERENCES

[1] S. Rangan, T. S. Rappaport, and E. Erkip, "Millimeter-wave cellular wireless networks: Potentials and challenges," *Proc. IEEE*, vol. 102, no. 3, pp. 366–385, Mar. 2014.

[2] M. Xiao *et al.*, "Millimeter wave communications for future mobile networks," *IEEE J. Sel. Areas Commun.*, vol. 35, no. 9, pp. 1909–1935, Sep. 2017.

[3] R. Olsen and A. Farstad, "Electromagnetic direction finding experiments for location of trapped miners," *IEEE Trans. Geosci. Electron.*, vol. 11, no. 4, pp. 178–185, Oct. 1973.

[4] A. Giere, P. Scheele, Y. Zheng, and R. Jakoby, "Characterization of the field-dependent permittivity of nonlinear ferroelectric films using tunable coplanar lines," *IEEE Microw. Wireless Compon. Lett.*, vol. 17, no. 6, pp. 442–444, Jun. 2007.

[5] A.-L. Franc, O. H. Karabey, G. Rehder, E. Pistono, R. Jakoby, and P. Ferrari, "Compact and broadband millimeter-wave electrically tunable phase shifter combining slow-wave effect with liquid crystal technology," *IEEE Trans. Microw. Theory Techn.*, vol. 61, no. 11, pp. 3905–3915, Nov. 2013.

[6] E. A. Firouzjaei, *mm-Wave Phase Shifters and Switches*. Berkeley, CA, USA: Univ. California, 2010.

[7] R. Amirkhanzadeh, "High resolution integrated passive phase shifters for future wireless communications," Ph.D. dissertation, Victoria Univ., Footscray, VIC, Australia, 2015.

[8] W. Zhu *et al.*, "A 21 to 3 GHz merged digital-controlled high resolution phase shifter-programmable gain amplifier with orthogonal phase and gain control for 5G phase array application," in *Proc. IEEE Radio Freq. Integr. Circuits Symp.*, 2019, pp. 67–70.

[9] A. Basaligheh, P. Saffari, S. R. Boroujeni, I. Filanovsky, and K. Moez, "A 28–30 GHz CMOS reflection-type phase shifter with full 360 phase shift range," *IEEE Trans. Circuits Syst. II, Exp. Briefs*, vol. 67, no. 11, pp. 2452–2456, Nov. 2020.

[10] G. McFeetors and M. Okoniewski, "Distributed MEMS analog phase shifter with enhanced tuning," *IEEE Microw. Wireless Compon. Lett.*, vol. 16, no. 1, pp. 34–36, Jan. 2006.

[11] G.-S. Shin *et al.*, "Low insertion loss, compact 4-bit phase shifter in 65 nm CMOS for 5G applications," *IEEE Microw. Wireless Compon. Lett.*, vol. 26, no. 1, pp. 37–39, Jan. 2016.

[12] Z. R. Omam, A. Pourziad, W. M. Abdel-Wahab, S. Nikmehr, S. Gigoyan, and S. Safavi-Naeini, "Two-way tunable phase shifter with arbitrary phase shift ratio at two different frequencies," *IEEE Trans. Microw. Theory Techn.*, vol. 68, no. 2, pp. 711–720, Feb. 2020.

[13] L. M. Blinov, *Structure and Properties of Liquid Crystals*, vol. 123. Berlin, Germany: Springer-Verlag, 2010.

[14] F. H. Raab, E. B. Blood, T. O. Steiner, and H. R. Jones, "Magnetic position and orientation tracking system," *IEEE Trans. Aerosp. Electron. Syst.*, vol. AES-15, no. 5, pp. 709–718, Sep. 1979.

[15] F. Goelden, S. Mueller, P. Scheele, M. Wittek, and R. Jakoby, "IP3 measurements of liquid crystals at microwave frequencies," in *Proc. Eur. Microw. Conf.*, 2006, pp. 971–974.

[16] M. Nickel *et al.*, "Ridge gap waveguide based liquid crystal phase shifter," *IEEE Access*, vol. 8, pp. 77833–77842, 2020.

[17] L. Cai, H. Xu, J. Li, and D. Chu, "High figure-of-merit compact phase shifters based on liquid crystal material for 1–10 GHz applications," *Jpn. J. Appl. Phys.*, vol. 56, no. 1, 2016, Art. no. 011701.
[18] Y. Poplavko *et al.*, "Low loss microwave piezo-tunable devices," in *Proc. Eur. Microw. Conf.*, 2006, pp. 657–660.
[19] O. H. Karabey, A. Gaebler, S. Strunck, and R. Jakoby, "A 2-D electronically steered phased-array antenna with 2 × 2 elements in LC display technology," *IEEE Trans. Microw. Theory Techn.*, vol. 60, no. 5, pp. 1297–1306, May 2012.
[20] F. Goelden, A. Gaebler, M. Goebel, A. Manabe, S. Mueller, and R. Jakoby, "Tunable liquid crystal phase shifter for microwave frequencies," *Electron. Lett.*, vol. 45, no. 13, pp. 686–687, 2009.
[21] S. Bulja, D. Mirshekar-Syahkal, R. James, S. E. Day, and F. A. Fernández, "Measurement of dielectric properties of nematic liquid crystals at millimeter wavelength," *IEEE Trans. Microw. Theory Techn.*, vol. 58, no. 12, pp. 3493–3501, Dec. 2010.
[22] D.-K. Yang and S.-T. Wu, *Fundamentals of Liquid Crystal Devices*. Hoboken, NJ, USA: Wiley, 2014.
[23] D. M. Pozar, *Microwave Engineering USA*. Hoboken, NJ, USA: Wiley, 2009.
[24] M. J. Rodwell *et al.*, "Active and nonlinear wave propagation devices in ultrafast electronics and optoelectronics," *Proc. IEEE*, vol. 82, no. 7, pp. 1037–1059, Jul. 1994.
[25] N. S. Barker and G. M. Rebeiz, "Optimization of distributed MEMS transmission-line phase shifters-U-band and W-band designs," *IEEE Trans. Microw. Theory Techn.*, vol. 48, no. 11, pp. 1957–1966, Nov. 2000.
[26] M. Himdi, J. Daniel, and C. Terret, "Transmission line analysis of aperture-coupled microstrip antenna," *Electron. Lett.*, vol. 25, no. 18, pp. 1229–1230, 1989.
[27] C. A. Balanis, *Antenna Theory: Analysis and Design*. Hoboken, NJ, USA: Wiley, 2015.
[28] C.-S. Lin, S.-F. Chang, and W.-C. Hsiao, "A full-360° reflection-type phase shifter with constant insertion loss," *IEEE Microw. Wireless Compon. Lett.*, vol. 18, no. 2, pp. 106–108, Feb. 2008.
[29] Y. Huang, J. Bao, X. Li, Y. Wang, and Y. Du, "A 4-bit switched-line phase shifter based on MEMS switches," in *Proc. 10th IEEE Int. Conf. Nano/Micro Engineered Mol. Syst.*, 2015, pp. 405–408.
[30] W. W. Hui, J. M. Bell, M. F. Iskander, and J. Lee, "Low-cost microstrip-line-based ferrite phase shifter design for phased array antenna applications," *IEEE Antennas Wireless Propag. Lett.*, vol. 6, pp. 86–89, 2007.
[31] D. Wang *et al.*, "Fast and miniaturized phase shifter with excellent figure of merit based on liquid crystal and nanowire-filled membrane technologies," *IEEE J. Microwaves*, vol. 2, no. 1, pp. 174–184, Jan. 2022.
[32] H. Tesmer *et al.*, "Feasibility of additively manufactured tunable liquid crystal loaded dielectric waveguides," *IEEE Microw. Wireless Compon. Lett.*, vol. 31, no. 8, pp. 973–976, Aug. 2021.
[33] X. Y. Li, D. Jiang, J. Liu, and M. Tong, "A Ka-band multilayer beaming-scanning antenna using liquid crystals," *IEEE Antennas Wireless Propag. Lett.*, vol. 21, no. 1, pp. 44–48, Jan. 2022.
[34] D. Wang, E. Polat, H. Tesmer, R. Jakoby, and H. Maune, "A compact and fast 1 × 4 continuously steerable endfire phased-array antenna based on liquid crystal," *IEEE Antennas Wireless Propag. Lett.*, vol. 20, no. 10, pp. 1859–1862, Oct. 2021.

MOHAMMAD ALI PANAHI received the B.S. degree from the Isfahan University of Technology, Isfahan, Iran, in 2013, and the M.S. degree from the University of Tehran, Tehran, Iran, in 2015. He is currently working toward the Ph.D. degree with the Department of Electrical and Computer Engineering, University of California at Los Angeles, Los Angeles, CA, USA.

His research interests include RF and microwave component and system including RFIC, phased array receiver and transmitter, RF power amplifier, phase shifter, and antenna array.

LAP YEUNG (Member, IEEE) received the B.Eng. degree in electrical and information engineering from the University of Sydney, Sydney, NSW, Australia, in 1998, the M.Eng. degree in electronic engineering from the Chinese University of Hong Kong, Hong Kong, in 2002, and the Ph.D. degree in electrical engineering from the University of California at Los Angeles, Los Angeles, CA, USA, in 2009. In 1999, he was with the Commonwealth Scientific and Industrial Research Organization, Sydney, Australia, where he was a Research Engineer involved in the numerical modeling of different antenna structures. From 2003 to 2006, he was with the Chinese University of Hong Kong, where he was involved in various LTCC multichip module designs and the development of numerical algorithms for analyzing multilayer embedded RF modules.

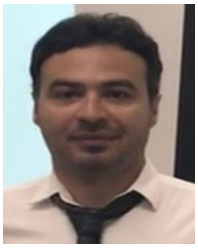

MAZIAR HEDAYATI received the B.S. degree in electrical engineering from the Isfahan University of Technology, Isfahan, Iran, in 2011. He is currently working toward the Ph.D. degree with the University of California at Los Angeles (UCLA), Los Angeles, CA, USA.

He was a Research Assistant with the Antenna and Microwave Lab, Isfahan University of Technology. In 2017, he joined Digital Microwave Laboratory, UCLA. His research interests include distributed transmit beamforming, phased antenna arrays, RFIC, antenna, and microwave.

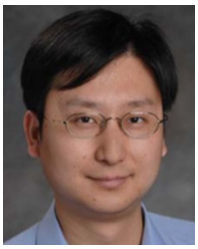

YUANXUN ETHAN WANG (Fellow, IEEE) received the B.S. degree in electrical engineering from the University of Science and Technology of China, Hefei, China, in 1993, and the M.S. and Ph.D. degrees in electrical engineering from The University of Texas at Austin, Austin, TX, USA, in 1996 and 1999, respectively.

In November 2002, he became an Assistant Professor with the Department of Electrical and Computer Engineering, University of California at Los Angeles, Los Angeles, CA, USA, where he is currently a Full Professor, and also the Director of the Digital Microwave Laboratory and the Center for High Frequency Electronics. He has authored more than 200 journal and conference articles. His research focuses on microwave systems. His expertise ranges from system to devices. His researches blend digital technologies and concepts into RF design, which often leads to novel devices with performances beyond the conventional bound.

Prof. Wang was the co-recipient of the First Place Best Student Paper in the 2017 International Microwave Symposium and Best Student Paper Award in the 2017 GOMAC Tech Symposium. He was an Associate Editor for IEEE TRANSACTIONS ON ANTENNAS AND PROPAGATION.